How Valley-Orbit States in Silicon Quantum Dots Probe Quantum Well Interfaces

J. P. Dodson,[1] H. Ekmel Ercan,[1] J. Corrigan,[1] Merritt P. Losert,[1] Nathan Holman,[1] Thomas McJunkin,[1] L. F. Edge,[2]
Mark Friesen,[1] S. N. Coppersmith,[1,3] and M. A. Eriksson[1]

[1]*Department of Physics, University of Wisconsin-Madison, Madison, Wisconsin 53706, USA*
[2]*HRL Laboratories, LLC, 3011 Malibu Canyon Road, Malibu, California 90265, USA*
[3]*University of New South Wales, Sydney, New South Wales 2052, Australia*

The energies of valley-orbit states in silicon quantum dots are determined by an as yet poorly understood interplay between interface roughness, orbital confinement, and electron interactions. Here, we report measurements of one- and two-electron valley-orbit state energies as the dot potential is modified by changing gate voltages, and we calculate these same energies using full configuration interaction calculations. The results enable an understanding of the interplay between the physical contributions and enable a new probe of the quantum well interface.

The ability to make uniform and tunable qubits is crucial for large-scale applications. Modern computers use one control electrode per field effect transistor with excellent uniformity, and proposed architectures for quantum chips also rely on a small number of control lines per qubit, in order to minimize the density of control wires [1,2]. Progress has recently been made enhancing the homogeneity of the electrical environment by using quantum dot designs that eliminate modulation doping and instead make use of metal surface electrodes to both accumulate and deplete electrons [3]. The resulting structures enable good control over electron occupation, gate voltages, and tunnel couplings between quantum dots with a small number of gate electrodes per quantum dot [4–11].

Uniformity remains a challenge in regard to conduction band valley energies in silicon [12,13], and important physical questions need to be addressed. Atomistic disorder is known to play a particularly important (and typically uncontrolled) role in determining the energies of electrons at the bottom of the valleys [14–19], resulting in a wide range of observed valley splittings in Si/SiGe quantum dots ($20-270$ μeV [20–29]). Critically, the interplay between the factors that determine the valley splitting in quantum dots—the atomic details of the interface (which vary with lateral position), the degree of lateral confinement, and electron-electron interactions within a quantum dot—are not yet fully understood.

This Letter reports quantitative characterization of the relationship between low-lying one- and two-electron valley-orbit states and the quantum dot confinement strength, shape, and position. The pulsed-gate spectroscopy and magnetospectroscopy measurements reveal valley splittings in the range $36-87$ μeV, two-electron singlet-triplet splittings between $22-59$ μeV, and orbital splittings that can be tuned from 1.69 to 2.26 meV. Simulations

combining full configuration interaction (FCI) [30] with empirical tight-binding theory [31] are shown to be in good agreement with the experimental results, and together these methods enable an understanding of the interplay between effects arising from quantum well interface roughness, orbital confinement strength, and electron-electron (e-e) interactions. This combination of experiment and theory not only explains the origin of the energy spectrum but also provides a new method for probing the quantum well interface.

Spectroscopy of one- and two-electron valley-orbit states is performed in a device fabricated using a three-layer overlapping aluminum gate architecture [3], as shown in Fig. 1(a). A detailed fabrication process can be found in Ref. [7]. The integrated sensor dot under gate M measures the electron occupation of the central quantum dot under gate $P2$. The triple dot on the bottom side is tuned into a regime where $B1$ and $P1$ form a large tunnel barrier on the left side of $P2$, suppressing the tunnel rate into reservoir $R3$. Gates $P3$ and $B4$ extend the reservoir $R4$ into the quantum dot channel, as shown by the electron density heat map in Fig. 1(b), allowing for the tunnel barrier beneath gate $B3$ to tune the tunnel coupling between the $P2$ dot and right reservoir under $R4$. Screening gates $S1$, $S2$, and $S3$ control the y confinement of the $P2$ dot. The electron temperature is measured to be $T_e = 100$ mK.

One- and two-electron valley-orbit splittings are measured by pulsed-gate spectroscopy using the experimental setup shown in Fig. 1(c). A 50% duty cycle square voltage pulse with amplitude V_{pulse} and frequency f_{pulse} is applied to gate $P2$, pulsing the ground state of the quantum dot between two levels: E_{Lg} and $E_{\text{Ug}} = E_{\text{Lg}} + \alpha V_{\text{pulse}}$, where E_{Lg} (E_{Ug}) denotes the ground state of the dot in the loading (unloading) position, and α is the lever arm for gate $P2$. A measurable change in the average electron occupation of
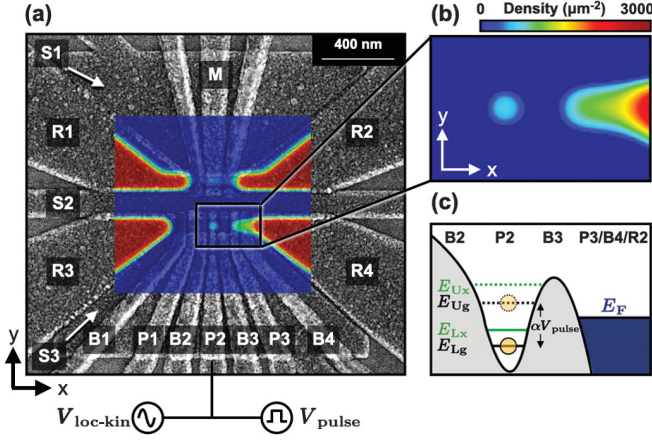
FIG. 1. Device layout and experimental setup. (a) A scanning electron microscope (SEM) image of a device lithographically identical to the one measured shows the gate electrode layout in the active region. A COMSOL MULTIPHYSICS Thomas-Fermi simulation of the electron density is overlaid on the SEM image. The sensor dot under gate M measures the average charge occupation $\langle n \rangle$ of the $P2$ quantum dot via lock-in amplifier detection at frequency $f_{\text{lock-in}}$. (b) The COMSOL simulation shows the charge density of the $P2$ dot, where the tunnel barrier to the left (right) reservoir is opaque (transparent). (c) Valley-orbit state splittings are measured using pulsed-gate spectroscopy. A 50% duty cycle square pulse with amplitude V_{pulse} at frequency f_{pulse} is applied to gate $P2$, rapidly pulsing the chemical potential of the $P2$ dot between E_{Lg} and E_{Ug}. The change in chemical potential induces detectable shifts in the tunnel rate into and out of the $P2$ quantum dot, allowing for measurement of excited state energies.

the dot $\langle n \rangle$ occurs when an excited state provides an additional channel for the electron to enter the dot, yielding a measurement of the energy of this excited state [32–34].

Figures 2(a) and 2(b) show pulsed-gate spectroscopy measurements of the one-electron E_{orb} at $V_{S3} = 390$ mV. Differential conductance measurements, reported as dg_M/dV_{P2} are used to determine the location of excited states at particular gate voltages. The excited orbital state is separated well enough from the ground state such that each peak position is found by fitting to the derivative of a Fermi function [35,36], where $E_{\text{orb}} = \alpha \Delta V_{\text{orb}}$. As shown in Figs. 2(c) and 2(d), a similar procedure is used to measure the valley splitting at $V_{S3} = 380$ mV, which is easily differentiated from the orbital splitting since it is much lower lying in energy. In this case, there is overlap of the ground and lowest excited state signals that arise from thermal broadening. To extract the peak locations, we make use of an expression for $\langle n \rangle$,

$$\langle n \rangle = \sum_{i=g,x} \Gamma_i \frac{e^{(E_i - E_F)/E_{0i}}}{e^{(E_i - E_F)/k_B T_e} + 1}, \tag{1}$$

where $E_i = \alpha V_i$ is the position of each peak in energy, and E_{0i} and Γ_i are fitting parameters for each peak. As shown
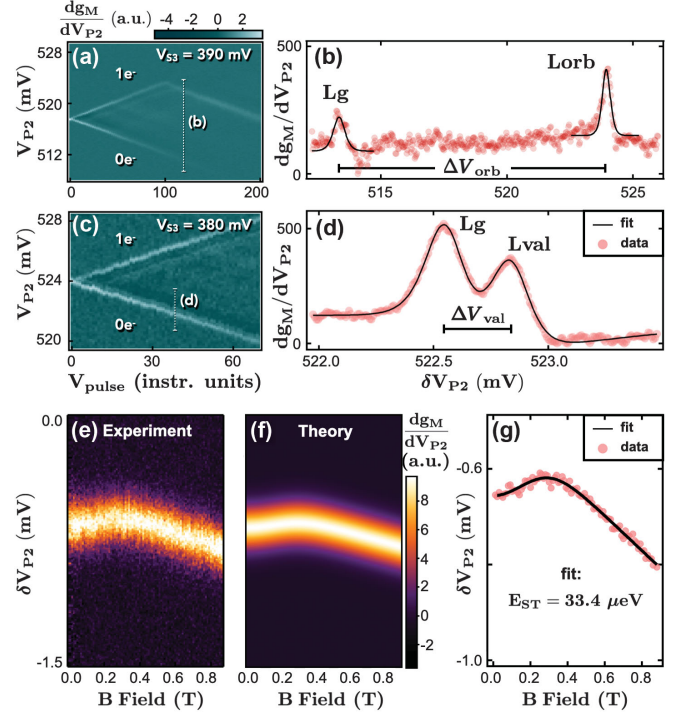

FIG. 2. Experimental methods. (a),(b) Measurement of orbital splitting using pulsed-gate spectroscopy. The pulse amplitude is increased until the lowest-lying orbital state is visible, shown in (a). A line cut (dashed line) is taken when the pulse amplitude exceeds the orbital splitting, allowing detection of the ground (L_g) and excited orbital (L_{orb}) states, shown as the peaks in (b). The orbital splitting is given by $\alpha \Delta V_{\text{orb}}$. (c),(d) Using the same method, the valley (E_{val}) and singlet-triplet splittings (E_{ST}) are measured. The red data points clearly show two distinct peaks in (d). The data are fit using Eq. (1), shown as the black line, giving $E_{\text{val}} = \alpha \Delta V_{\text{val}} = 53.2$ μeV. (e)–(g) Experimental magnetospectroscopy data (e) are reproduced in (f) by treating the dot-reservoir system as a grand canonical ensemble. The experimental peak locations in voltage space are extracted from (e) and plotted in (g) as red circles, which are then fit to Eq. (2), yielding $E_{\text{ST}} = 33.4$ μeV.

by the solid line in Fig. 2(d), the experimental data are fit by the derivative of Eq. (1) with respect to the gate voltage ($d\langle n \rangle/dV_{P2}$), enabling extraction of $E_{\text{val}} = \alpha \Delta V_{\text{val}}$.

The two-electron singlet-triplet splitting (E_{ST}) is measured using both pulsed-gate spectroscopy (using a similar procedure as above) and magnetospectroscopy, as shown in Figs. 2(e)–2(g). The latter is performed by adiabatically sweeping across the $1 \rightarrow 2$ charge transition line and measuring the resulting position of the charge transition peak. Measurements of E_{ST} using each of these methods are shown to be in agreement in Sec. S3 of the Supplemental Material [37]. This method is described in further detail in Refs. [22,23,47,48]. A full theoretical model for magnetospectroscopy is developed in the Supplemental Material, which allows for the experimental data shown in Fig. 2(e) to be closely reproduced by the model in Fig. 2(f).

This model enables fitting the peak position of the data in Fig. 2(e), using

$$V_{P2}(B) = \frac{1}{\alpha\beta_e} \ln\left(\frac{e^{\frac{1}{2}\kappa B + \beta_e E_{ST}}(e^{\kappa B} + 1)}{e^{\kappa B} + e^{2\kappa B} + e^{\kappa B + \beta_e E_{ST}} + 1}\right), \quad (2)$$

where V_{P2} is the gate voltage, $\kappa = g\mu_B\beta_e$ where $\beta_e = 1/k_B T_e$, g is the electron g factor, μ_B is the Bohr magneton, and B is the magnetic field. The peak positions from Fig. 2(e) are extracted and plotted as red circles in Fig. 2(g), and the fit (solid line) to Eq. (2) yields for this example $E_{ST} = 33.4\ \mu\text{eV}$.

We now show that, by combining these two different spectroscopic techniques and by combining two different theoretical techniques, we can extract a quantitative measure of the suppression of the singlet-triplet splitting from the valley splitting. Further, below we show that these same techniques allow us to extract information about the atomic details of the interface by comparing measurement of E_{val}, E_{ST}, and E_{orb} vs electrostatic confinement in the x–y plane. The confinement is varied by changing the $S3$ gate voltage (V_{S3}) between 260–420 mV while compensating with neighboring barrier and plunger gates to maintain a constant electron occupation and tunnel rate into the dot.

Figure 3 shows the effects of changing V_{S3} on quantum dot orbital energy, shape, and position. The device schematic pictured in the top left inset shows the approximate location of the $P2$ dot as the shaded blue region. Changes to the voltage V_{S3} applied to the screening gate, shown as the shaded gray region in the inset, modify the $P2$ dot confinement, orbital shape, and position. The minimum orbital splitting, plotted as solid circles in Fig. 3, is found to be nonmonotonic with V_{S3}, because of the strong effect $S3$ has on the electrostatic confinement of the dot along the y axis. At high V_{S3}, the y confinement becomes weak, and the minimum orbital splitting falls off rapidly due to elongation of the dot along the y axis. Toward the center, the dot becomes isotropic, increasing the minimum orbital splitting up to 2.26 meV at $V_{S3} = 370$ mV. At low V_{S3}, suppression of the minimum orbital splitting occurs due to the compensating barrier and plunger gate voltages needed to stay in the one-electron regime, elongating the dot along the x axis. Since low V_{S3} creates a tight confinement potential along the y axis, the x orbital is the most weakly confined orbital below $V_{S3} = 370$ mV.

This behavior is well explained by semiclassical (Thomas-Fermi) electrostatic simulations using COMSOL MULTIPHYSICS, shown in the bottom inset of Fig. 3. The position and orbital shape are simulated at the four points indicated by the shaded purple circles from the experimental data. The outline of each oval represents the shape that encloses 50% of the electron wave function, and the small circles show the center of the electron density for each simulation. The Thomas-Fermi simulations qualitatively match the experimental findings, where the x orbital
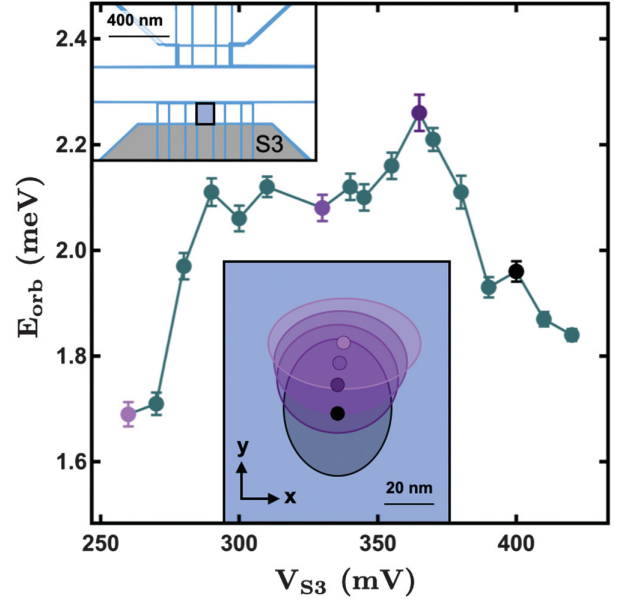

FIG. 3. Quantum dot orbital shape and position. The top left inset shows a device schematic where the $P2$ quantum dot is located within the filled blue region and the $S3$ gate is shown as the filled gray region. The minimum orbital splitting is plotted as a function of V_{S3}. At low V_{S3}, the dot has strong y confinement and weak x confinement, leading to a drop in the minimum orbital splitting. As V_{S3} is increased, the dot becomes isotropic, increasing the minimum orbital splitting. At high V_{S3}, the dot has weak y confinement and strong x confinement, reducing the minimum orbital splitting again. Thomas-Fermi electrostatic simulations are used to calculate the quantum dot shape and position within the blue region shown in the device schematic. Four points are simulated, shown as the shaded purple circles in the experimental data. The change in shape of the electron density is found to be in agreement with the experimental data. Additionally, the position of the quantum dot for each simulation is illustrated as the small solid circle in the inset, showing that the quantum dot slides down and to the left 23.8 nm.

is most weakly confined at low V_{S3} and the y orbital is most weakly confined at high V_{S3}. In addition to the changes in shape, significant change in the position of the dot is observed in the COMSOL simulations. Over the range shown, the quantum dot position slides down and to the left as V_{S3} increases for a total change in position of 23.8 nm. We note that COMSOL simulations were not used to determine the dot shape and position above 400 mV, because this regime becomes close to the accumulation threshold for the S3 gate, where uncertainties become large.

Atomic steps in the quantum well interface play an important role in determining E_{val} and E_{ST}. Figure 4(a) plots E_{val} (filled blue squares) and E_{ST} (filled red circles) as the orbital shape and dot position are varied with V_{S3}, where the shaded region represents the measurement uncertainty. The measured E_{val} and E_{ST} change substantially across the electrostatic configurations, and their large
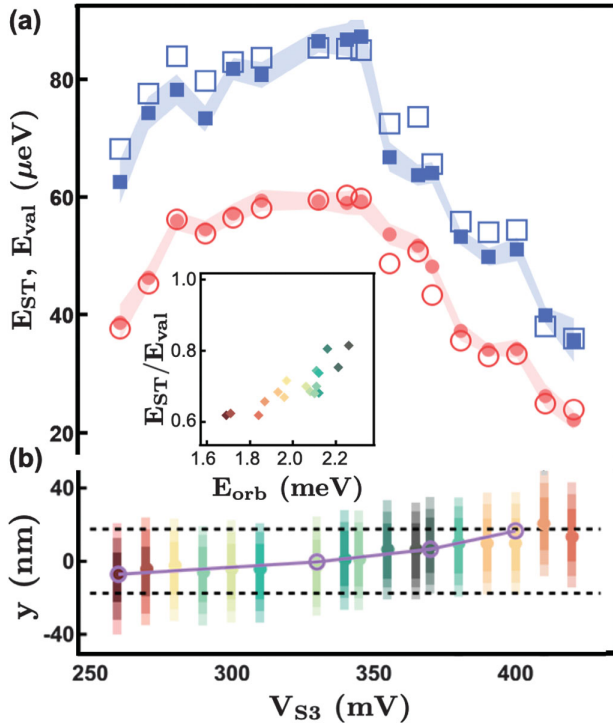
FIG. 4. (a) The measured valley splitting (E_{val}) and singlet-triplet splitting (E_{ST}) are plotted as a function of V_{S3} as filled blue squares and red circles, respectively, where the measurement uncertainty is indicated by the width of the shaded regions. FCI simulations for E_{val} and E_{ST}, shown as open blue squares and red circles, respectively, quantitatively reproduce the experimental data once the effects of disorder in the form of atomic steps at the quantum well interface are included. (b) The nonmonotonic behavior observed in both E_{ST} and E_{val} as a function V_{S3} is well explained by the quantum dot position changing with respect to distinct atomic steps at the quantum well interface. The wave function and position of the $P2$ dot singlet state is plotted with respect to atomic steps (dashed lines) at the interface, shown as the colored gradients and points. A best fit to the data produces a smooth change in position of the dot across steps spaced approximately 35 nm apart. The change in position from the Thomas-Fermi simulation, plotted as the purple line and open circles, agrees well with the FCI simulations. The inset plots the ratio E_{ST}/E_{val} as a function of the orbital splitting (E_{orb}), where the colored points map the magnitude of the orbital splitting to the position of the electron wave function with respect to atomic steps in (b). As seen in (b), the suppression of the ratio E_{ST}/E_{val} below unity is a consequence of strong electron-electron interactions dominated by the magnitude of the orbital splitting.

in situ tunability arises from motion of the $P2$ quantum dot with respect to atomic steps at the quantum well interface. As the dot approaches an atomic step, more of the wave function overlaps the step, thereby increasing the valley-orbit coupling that suppresses E_{val} and E_{ST} [49]. To determine the position of atomic steps relative to the quantum dot, we make use of a combination of the experimental measurements, the COMSOL simulations just described, and FCI calculations, the latter of which

incorporate valley-orbit coupling that arises from interface roughness. The FCI calculations use a single fitting parameter in order to match the measured values of E_{val} and E_{ST}, namely, the position of the dot relative to atomic steps at the quantum well interface.

Figure 4(a) shows the results of FCI calculations for E_{val} and E_{ST} as open blue squares and open red circles, respectively. Close agreement with the experimental data is found when the atomic steps are separated by 35 nm. The positions used in the FCI calculations to produce the best fit to the data at each point are plotted in Fig. 4(b) as solid colored points. Each point has a colored gradient overlay that represents the spatial extent of the singlet (ground) state with respect to the atomic steps, which are shown as black dashed lines. The gradient steps from darkest to lightest, corresponding to wave function probability thresholds of 75%, 50%, and 25% of its maximum value.

A linear fit to the dot positions calculated from the FCI simulations reveal a total change in position of the dot of 24.7 nm with respect to the axis perpendicular to the atomic steps in the interface, which is consistent with the change in position extracted from the COMSOL simulations: 23.8 nm. This correspondence is shown in Fig. 4(b), which shows the dot position from each of the four COMSOL simulations (purple open circles) overlaid on the calculated FCI wave function distributions (color gradients). The close agreement provides a measure of validation for an approach that allows an in situ method of probing the quantum well interface through a combination of spectroscopic measurements of the quantum dot and theoretical simulations. This is an important development since currently the only methods of probing atomic details of buried interfaces are destructive metrology techniques such as transmission electron microscopy, nanobeam x ray, or atom probe tomography [50–52]. We note that, in future work, more detailed information could be determined by moving the dot along two axes. In this experiment, the direction of the atomic steps with respect to the movement vector of the quantum dot cannot be determined.

The inset of Fig. 4(a) reports the ratio E_{ST}/E_{val} as a function of E_{orb}, showing that this ratio is significantly below unity for the entire range of parameters measured. Electron-electron interactions suppress E_{ST} below the noninteracting energy E_{val} [53,54], revealing that there are strong e-e interactions across all orbital splittings studied here (1.69–2.26 meV). To look for any correlations between dot position relative to the steps and the ratio E_{ST}/E_{val}, the dot positions in Fig. 4(b) are color coded by their corresponding orbital energies, with the mapping shown in the inset plot. The colors of the data points map the magnitude of the orbital splitting to the distance of the dot from an atomic step. The random distribution of colors in Fig. 4(b) demonstrates that there is very little correlation between the distances of the dot from an atomic

step and the orbital splitting. Thus, the orbital splitting is more important than dot position in determining the suppression of E_{ST} below its noninteracting limit of E_{val}.

In summary, we measure large *in situ* tunability of valley, singlet-triplet, and orbital splittings, allowing for determination of the quantitative relationship between these three important energy scales. FCI simulations of the measured valley-orbit states were found to be in good agreement with the data, pointing to a combination of two primary physical parameters driving the relationship between these valley-orbit states: electrostatic confinement strength and quantum dot position relative to steps in the quantum well interface. This improved understanding enables a new *in situ* method of probing the quantum well interface through a combination of spectroscopic data and theoretical simulations.

[1] L. Vandersypen, H. Bluhm, J. Clarke, A. Dzurak, R. Ishihara, A. Morello, D. Reilly, L. Schreiber, and M. Veldhorst, npj Quantum Inf. **3**, 34 (2017).

[2] M. Veldhorst, H. Eenink, C.-H. Yang, and A. S. Dzurak, Nat. Commun. **8**, 1766 (2017).

[3] D. M. Zajac, T. M. Hazard, X. Mi, E. Nielsen, and J. R. Petta, Phys. Rev. Applied **6**, 054013 (2016).

[4] D. M. Zajac, A. J. Sigillito, M. Russ, F. Borjans, J. M. Taylor, G. Burkard, and J. R. Petta, Science **359**, 439 (2018).

[5] X. Mi, M. Benito, S. Putz, D. M. Zajac, J. M. Taylor, G. Burkard, and J. R. Petta, Nature (London) **555**, 599 (2018).

[6] S. F. Neyens, E. R. MacQuarrie, J. P. Dodson, J. Corrigan, N. Holman, B. Thorgrimsson, M. Palma, T. McJunkin, L. F. Edge, M. Friesen, S. N. Coppersmith, and M. A. Eriksson, Phys. Rev. Applied **12**, 064049 (2019).

[7] J. P. Dodson, N. Holman, B. Thorgrimsson, S. F. Neyens, E. F. MacQuarrie, T. McJunkin, R. H. Foote, L. F. Edge, S. N. Coppersmith, and M. A. Eriksson, Nanotechnology **31**, 505001 (2020).

[8] A. Mills, D. Zajac, M. Gullans, F. Schupp, T. Hazard, and J. Petta, Nat. Commun. **10**, 1063 (2019).

[9] R. W. Andrews, C. Jones, M. D. Reed, A. M. Jones, S. D. Ha, M. P. Jura, J. Kerckhoff, M. Levendorf, S. Meenehan, S. T. Merkel, A. Smith, B. Sun, A. J. Weinstein, M. T. Rakher, T. D. Ladd, and M. G. Borselli, Nat. Nanotechnol. **14**, 747 (2019).

[10] N. Holman, J. Dodson, L. Edge, S. Coppersmith, M. Friesen, R. McDermott, and M. Eriksson, Appl. Phys. Lett. **117**, 083502 (2020).

[11] K. Takeda, A. Noiri, T. Nakajima, J. Yoneda, T. Kobayashi, and S. Tarucha, Nat. Nanotechnol. **16**, 965 (2021).

[12] T. Ando, A. B. Fowler, and F. Stern, Rev. Mod. Phys. **54**, 437 (1982).

[13] T. B. Boykin, G. Klimeck, M. A. Eriksson, M. Friesen, S. N. Coppersmith, P. von Allmen, F. Oyafuso, and S. Lee, Appl. Phys. Lett. **84**, 115 (2004).

[14] M. Friesen, M. A. Eriksson, and S. N. Coppersmith, Appl. Phys. Lett. **89**, 202106 (2006).

[15] N. Kharche, M. Prada, T. B. Boykin, and G. Klimeck, Appl. Phys. Lett. **90**, 092109 (2007).

[16] D. Culcer, X. Hu, and S. Das Sarma, Phys. Rev. B **82**, 205315 (2010).

[17] J. K. Gamble, M. A. Eriksson, S. N. Coppersmith, and M. Friesen, Phys. Rev. B **88**, 035310 (2013).

[18] P. Boross, G. Széchenyi, D. Culcer, and A. Pályi, Phys. Rev. B **94**, 035438 (2016).

[19] A. Hosseinkhani and G. Burkard, Phys. Rev. Research **2**, 043180 (2020).

[20] N. Shaji, C. B. Simmons, M. Thalakulam, L. J. Klein, H. Qin, H. Luo, D. E. Savage, M. G. Lagally, A. J. Rimberg, R. Joynt, M. Friesen, R. H. Blick, S. N. Coppersmith, and M. A. Eriksson, Nat. Phys. **4**, 540 (2008).

[21] C. B. Simmons, T. S. Koh, N. Shaji, M. Thalakulam, L. J. Klein, H. Qin, H. Luo, D. E. Savage, M. G. Lagally, A. J. Rimberg, R. Joynt, R. Blick, M. Friesen, S. N. Coppersmith, and M. A. Eriksson, Phys. Rev. B **82**, 245312 (2010).

[22] Z. Shi, C. B. Simmons, J. Prance, J. K. Gamble, M. Friesen, D. E. Savage, M. G. Lagally, S. N. Coppersmith, and M. A. Eriksson, Appl. Phys. Lett. **99**, 233108 (2011).

[23] M. G. Borselli, R. S. Ross, A. A. Kiselev, E. T. Croke, K. S. Holabird, P. W. Deelman, L. D. Warren, I. Alvarado-Rodriguez, I. Milosavljevic, F. C. Ku, W. S. Wong, A. E. Schmitz, M. Sokolich, M. F. Gyure, and A. T. Hunter, Appl. Phys. Lett. **98**, 123118 (2011).

[24] D. Kim, Z. Shi, C. B. Simmons, D. R. Ward, J. R. Prance, T. S. Koh, J. K. Gamble, D. E. Savage, M. G. Lagally, M. Friesen, S. N. Coppersmith, and M. A. Eriksson, Nature (London) **511**, 70 (2014).

[25] J. S. Schoenfield, B. M. Freeman, and H. Jiang, Nat. Commun. **8**, 64 (2017).

[26] X. Mi, C. G. Péterfalvi, G. Burkard, and J. R. Petta, Phys. Rev. Lett. **119**, 176803 (2017).

[27] A. M. Jones, E. J. Pritchett, E. H. Chen, T. E. Keating, R. W. Andrews, J. Z. Blumoff, L. A. De Lorenzo, K. Eng, S. D. Ha, A. A. Kiselev, S. M. Meenehan, S. T. Merkel, J. A. Wright, L. F. Edge, R. S. Ross, M. T. Rakher, M. G. Borselli, and A. Hunter, Phys. Rev. Applied **12**, 014026 (2019).

[28] A. Hollmann, T. Struck, V. Langrock, A. Schmidbauer, F. Schauer, T. Leonhardt, K. Sawano, H. Riemann, N. V. Abrosimov, D. Bougeard, and L. R. Schreiber, Phys. Rev. Applied **13**, 034068 (2020).

[29] E. H. Chen, K. Raach, A. Pan, A. A. Kiselev, E. Acuna, J. Z. Blumoff, T. Brecht, M. D. Choi, W. Ha, D. R. Hulbert, M. P. Jura, T. E. Keating, R. Noah, B. Sun, B. J. Thomas, M. G. Borselli, C. A. C. Jackson, M. T. Rakher, and R. S. Ross, Phys. Rev. Applied **15**, 044033 (2021).

[30] A. Szabo, *Modern Quantum Chemistry: Introduction to Advanced Electronic Structure Theory (Dover Books on Chemistry)* (Dover Publications, New York, 1996).

[31] T. B. Boykin, G. Klimeck, M. Friesen, S. N. Coppersmith, P. vonAllmen, F. Oyafuso, and S. Lee, Phys. Rev. B **70,** 165325 (2004).

[32] J. M. Elzerman, R. Hanson, L. H. Willems van Beveren, L. M. K. Vandersypen, and L. P. Kouwenhoven, Appl. Phys. Lett. **84,** 4617 (2004).

[33] C. H. Yang, W. H. Lim, N. S. Lai, A. Rossi, A. Morello, and A. S. Dzurak, Phys. Rev. B **86,** 115319 (2012).

[34] J. K. Gamble, P. Harvey-Collard, N. T. Jacobson, A. D. Baczewski, E. Nielsen, L. Maurer, I. Montaño, M. Rudolph, M. Carroll, C. Yang, A. Rossi, A. Dzurak, and R. P. Muller, Appl. Phys. Lett. **109,** 253101 (2016).

[35] M. Field, C. G. Smith, M. Pepper, D. A. Ritchie, J. E. F. Frost, G. A. C. Jones, and D. G. Hasko, Phys. Rev. Lett. **70,** 1311 (1993).

[36] L. P. Kouwenhoven, C. M. Marcus, P. L. McEuen, S. Tarucha, R. M. Westervelt, and N. S. Wingreen, Electron transport in quantum dots, in *Mesoscopic Electron Transport* (Kluwer, 1997), p. 105–214.

[37] See Supplemental Material at http://link.aps.org/supplemental/10.1103/PhysRevLett.128.146802 for the derivation of Eqs. (1) and (2), details of the COMSOL simulations, and details of the FCI calculations, which includes Refs. [38–46].

[38] N. E. Penthorn, J. S. Schoenfield, L. F. Edge, and H. W. Jiang, Phys. Rev. Applied **14,** 054015 (2020).

[39] K. MacLean, S. Amasha, I. P. Radu, D. M. Zumbühl, M. A. Kastner, M. P. Hanson, and A. C. Gossard, Phys. Rev. Lett. **98,** 036802 (2007).

[40] L. DiCarlo, H. J. Lynch, A. C. Johnson, L. I. Childress, K. Crockett, C. M. Marcus, M. P. Hanson, and A. C. Gossard, Phys. Rev. Lett. **92,** 226801 (2004).

[41] R. Hanson, L. P. Kouwenhoven, J. R. Petta, S. Tarucha, and L. M. K. Vandersypen, Rev. Mod. Phys. **79,** 1217 (2007).

[42] W. G. van der Wiel, S. De Franceschi, J. M. Elzerman, T. Fujisawa, S. Tarucha, and L. P. Kouwenhoven, Rev. Mod. Phys. **75,** 1 (2002).

[43] J. M. Elzerman, R. Hanson, J. S. Greidanus, L. H. Willems van Beveren, S. De Franceschi, L. M. K. Vandersypen, S. Tarucha, and L. P. Kouwenhoven, Phys. Rev. B **67,** 161308 (R) (2003).

[44] C. Kittel, H. Charles Kittel, K. Charles, H. Kroemer, and K. Herbert, *Thermal Physics* (W. H. Freeman, 1980).

[45] M. Stopa, Phys. Rev. B **54,** 13767 (1996).

[46] B. P. Wuetz, M. P. Losert, A. Tosato, M. Lodari, P. L. Bavdaz, L. Stehouwer, P. Amin, J. S. Clarke, S. N. Coppersmith, A. Sammak, M. Veldhorst, M. Friesen, and G. Scappucci, Phys. Rev. Lett. **125,** 186801 (2020).

[47] W. H. Lim, F. A. Zwanenburg, H. Huebl, M. Möttönen, K. W. Chan, A. Morello, and A. S. Dzurak, Appl. Phys. Lett. **95,** 242102 (2009).

[48] W. H. Lim, C. H. Yang, F. A. Zwanenburg, and A. S. Dzurak, Nanotechnology **22,** 335704 (2011).

[49] M. Friesen and S. N. Coppersmith, Phys. Rev. B **81,** 115324 (2010).

[50] T. McJunkin, E. R. MacQuarrie, L. Tom, S. F. Neyens, J. P. Dodson, B. Thorgrimsson, J. Corrigan, H. E. Ercan, D. E. Savage, M. G. Lagally, R. Joynt, S. N. Coppersmith, M. Friesen, and M. A. Eriksson, Phys. Rev. B **104,** 085406 (2021).

[51] J. A. Tilka, J. Park, Y. Ahn, A. Pateras, K. C. Sampson, D. E. Savage, J. R. Prance, C. B. Simmons, S. N. Coppersmith, M. A. Eriksson, M. G. Lagally, M. V. Holt, and P. G. Evans, J. Appl. Phys. **120,** 015304 (2016).

[52] O. E. Dyck, D. N. Leonard, L. Edge, C. Jackson, E. J. Pritchett, P. W. Deelman, and J. D. Poplawsky, Adv. Mater. Interf. **4,** 1700622 (2017).

[53] S. Pecker, F. Kuemmeth, A. Secchi, M. Rontani, D. C. Ralph, P. L. McEuen, and S. Ilani, Nat. Phys. **9,** 576 (2013).

[54] H. E. Ercan, S. N. Coppersmith, and M. Friesen, Phys. Rev. B **104,** 235302 (2021).